Applied Catalysis B: Environmental 142–143 (2013) 504–511

Contents lists available at SciVerse ScienceDirect

Applied Catalysis B: Environmental

journal homepage: www.elsevier.com/locate/apcatb

In situ synthesis of α–β phase heterojunction on Bi_2O_3 nanowires with exceptional visible-light photocatalytic performance

Jungang Hou, Chao Yang, Zheng Wang, Weilin Zhou, Shuqiang Jiao*, Hongmin Zhu

State Key Laboratory of Advanced Metallurgy, School of Metallurgical and Ecological Engineering, University of Science and Technology Beijing, Beijing 100083, China

ARTICLE INFO

Article history:
Received 29 January 2013
Received in revised form 26 April 2013
Accepted 22 May 2013
Available online 30 May 2013

Keywords:
Bismuth oxide
Charge transfer
Heterojunction
Photocatalysis

ABSTRACT

Visible-light-responsive α–β phase heterojunction on Bi_2O_3 nanowire photocatalysts were prepared via a facile in situ hydrothermal process in assistance with the post-heat treatment route. The as-prepared samples were characterized by X-ray diffraction (XRD), electron microscope (EM), Brunauer–Emmett–Teller analysis (BET), X-ray photoelectron spectroscopy (XPS), and UV–vis diffuse reflectance absorption spectra (UV–vis). XRD patterns revealed that the α–β phase heterojunction over Bi_2O_3 composites with the monoclinic α-Bi_2O_3 and the tetragonal β-Bi_2O_3 structure were obtained and the relative ratios between α-Bi_2O_3 and β-Bi_2O_3 can readily be tailored by the control of the reaction temperature. Within the hydrothermal temperature range, the morphology of as-prepared samples transformed progressively from two-dimensional β-Bi_2O_3 sheets to the α-/β-Bi_2O_3 nanowires junction. The exceptional photocatalytic performance of α-/β-Bi_2O_3 heterojunction for the degradation of cationic rhodamine B and anionic methyl orange under visible-light irradiation is superior over that of β-Bi_2O_3 sheets, which is ascribed to the efficient charge separation and transfer across the α-β phase junction. The phase-junction approach will open new avenues for the development of efficient photocatalysts for environmental remediation and energy conversion.

1. Introduction

Photocatalyst is a research topic of great importance in view of its applications in energy production, global environmental pollutant control, and final chemical synthesis. Many oxide semiconductors, such as TiO_2, ZnO, WO_3 and Ta_2O_5, have been employed as photocatalysts in pollutant degradation and water splitting reactions [1–4]. To date, TiO_2, as a semiconductor photocatalyst with large band gap (about 3.2 eV), has been intensively investigated under UV irradiation (λ < 388 nm). However, titania can only absorb about less than 5% of sunlight, which greatly limits its practical application [1]. Recently, TiO_2 has been modified by transition-metal cations, non-metal anions (such as N, S, C, F) or noble metal nanoparticles for the improvement of the catalytic performance in the visible range [5–8]. Among them, the Bi-based multimetal oxides with a $6s^2$ configuration, such as $CaBi_2O_4$ [9], $BiVO_4$ [10], Bi_2WO_6 [11], Bi_3NbO_7 [12,13] and $Bi_{12}TiO_{20}$ [14–18], have shown to be active under visible illumination, which can be ascribed to the fresh-constructed, well-dispersed valence bands by the hybridization of Bi 6s and O 2p orbitals [19,20].

Recently, Bi_2O_3 as an undoped and single oxide semiconductor sensitive to visible irradiation has been found to exhibit high photocatalytic performance due to the appropriate band gap [21]. As is known, Bi_2O_3 has four different polymorphs, denoted as monoclinic α, tetragonal β, body-centered cubic γ, and face-centered cubic δ, among which, the low-temperature α-phase and the high-temperature δ-phase are stable; while the other two phases are high-temperature metastable [22]. Though many researches on α-Bi_2O_3 have been reported, there were only a few on β-Bi_2O_3, in most of which β-Bi_2O_3 was obtained due to the difficulty of the synthesis of this metastable phase [23–26]. Generally, β-Bi_2O_3 showed higher photocatalytic activity than α-Bi_2O_3 owing to the lower band gap energy and higher optic absorption in wider visible light region [26–30]. Besides, Muruganandham et al. have successfully used two types of bismuth oxalates as a precursor for various morphological Bi_2O_3 preparations [31]. Chen et al. prepared bismuth oxide nanoflakes by using bismuth oxalate as a precursor with and without using L-lysine [32]. Brezesinski et al. found that the mesoporous β-Bi_2O_3 showed exceptional photocatalytic activity [33]. Thus, it is therefore highly desirable to develop a new modification and/or preparation method that can enhance the photocatalytic activity of Bi_2O_3.

* Corresponding author. Tel.: +86 10 62334204.
E-mail address: sjiao@ustb.edu.cn (S. Jiao).

0926-3373
http://dx.doi.org/10.1016/j.apcatb.2013.05.050

Generally, the photocatalytic performance of β-Bi_2O_3 is better than that of α-Bi_2O_3, because β-Bi_2O_3 could absorb more visible light than α-Bi_2O_3, which was explained by electronic structure calculations and experimental evidence [26–30]. To further improve the photocatalytic performance of Bi_2O_3 under the irradiation of solar light, different hybrid semiconductor heterostructures have been explored. Large numbers of efficient heterostructures for photocatalytic application are reported. For example, three-dimensional flower-like hierarchical Fe_2O_3@Bi_2O_3 architectures synthesized by a simple solvothermal route showed higher photocatalytic activity [34]. The Bi_2O_3/TiO_2/graphene hybrids have been applied as stable photocatalysts for the high photocatalytic activity for rhodamine B degradation [35]. The Bi_2O_3/N-Bi_3NbO_7 heterostructures prepared by a facile in situ hydrothermal process exhibited the higher photocatalytic activity [13]. Proper junctions formed in semiconductor-based photocatalysts could also lead to enhanced activity. However, fabricating efficient junctions for the photocatalytic reaction still remains a challenge. More importantly, the essential relation between the junction and the photocatalytic activity is far less well understood. An in-depth understanding of junction-related issues may be a great aid in the design and preparation of efficient semiconductor based photocatalysts.

In this work, the influences of synthesis parameters on the resulting products, the synthesis mechanism, the critical roles of treatment conditions and catalyst compositions in determining catalytic performance, as well as the contribution of the work to the fields of visible-light photocatalytic activities were elaborated in detail. There are several significant aspects of the work described in this paper. Firstly, the synthesis of shape-controlled β-Bi_2O_3 sheets to α-/β-Bi_2O_3 nanowire heterojunction have been found to be extremely evasive to date. Hence, the post-heat treatment route using bismuth based precursors through a facile hydrothermal process in assistance with benzyl alcohol as solvent should be an important progress that may inspire subsequent catalytic materials synthesis. Secondly, the exceptional photocatalytic performance of α-/β-Bi_2O_3 nanowire heterojunction for the degradation of cationic rhodamine B and anionic methyl orange under visible-light irradiation has been rarely reported. Hence, an in-depth understanding of junction-related issues may be a great aid in the design and preparation of efficient semiconductor based photocatalysts.

2. Experimental

2.1. Synthesis of α-/β-Bi_2O_3 nanostuctures

All chemicals were analytical grade and used without further purification. In a typical procedure, stochiometric amounts of $Bi(NO_3)_3{\cdot}5H_2O$ was dissolved in 15 mL of benzyl alcohol under vigorous stirring. Before being transferred to a Teflon-lined stainless autoclave (50 mL capacity). The hydrothermal synthesis was conducted at 90–240 °C for 24 h in an electric oven. The system was then cooled to ambient temperature naturally. The as-prepared samples as precursors were collected and washed with distilled water and absolute alcohol several times, vacuum-dried, and then heated at 300 °C for 5 h to obtain Bi_2O_3 nanostuctures.

2.2. Characterization

The obtained products were characterized by powder X-ray diffraction (XRD, MAC Science Co. Ltd Japan) using Cu Kα (λ = 0.1546 nm) and XRD patterns were obtained by step scanning with a step size of 0.02°. The morphology and size of the resultant products were observed using a field emission scanning electron microscope (FESEM, JEOL, JSM-6701F) with energy-dispersive spectra and transmission electron microscope (TEM, JEM-2010). The optical properties of the samples were analyzed by UV–vis diffuse reflectance spectroscopy (UV–vis DRS) using a UV–vis spectrophotometer (UV-2550, Shimadzu) in the range 190–900 nm. The surface area of the samples were measured by TriStar 3000-BET/BJH Surface Area. The chemical states of the sample were determined by X-ray photoelectron spectroscopy (XPS) in a VG Multilab 2009 system (UK) with a monochromatic Al Kα source and a charge neutralizer.

2.3. Photocatalytic test

Photocatalysis reactions were performed in an air-free, closed gas circulation system with a quartz reaction cell. Photocatalytic activity was evaluated by the degradation of methylene blue in aqueous solution under visible-light irradiation using a 300 W Xe lamp with a cutoff filter (λ > 420 nm). Light intensity and utilization efficiency is about 20 mW cm^{-2} and 95%, respectively. A cylindrical Pyrex flask (200 mL) was placed in a sealed black box of which the top was open and the cutoff filter was set on the window face of the reaction vessel to ensure the desired irradiation condition. In each experiments, the samples as catalysts (0.2 g) were added into rhodamine B (RhB) and methyl orange (MO) solution (1×10^{-4} M, 100 mL). Before illumination, the suspension between photocatalyst powders and methylene blue at given time intervals (3 mL aliquots) were sampled and centrifuged to remove photocatalyst powders. The various samples were taken out for the absorbance measurements using a UV–vis spectrophotometer (UV-2550, Shimadzu) and the TOC content in the aqueous solutions was analyzed using a TOC analyser (TOC-V CPH, Shimadzu).

2.4. Flatband potential measurements

The flatband potentials have been measured by impedance spectroscopy using Mott-Schottky plots. Individual α-Bi_2O_3 and β-Bi_2O_3 paste for the fabrication of electrodes for impedance measurements was obtained by mixing 1 mL of water and 100 mg of individual α-Bi_2O_3 and β-Bi_2O_3 powder (Supporting Information) homogeneously by sonication. An appropriate amount of the individual α-Bi_2O_3 and β-Bi_2O_3 suspension was spread on a conductive fluorine-tin oxide (FTO) glass with a glass rod, using adhesive tapes as spacers followed by drying in air at 300 °C for 1 h. The electrical contact was formed on the uncoated area of the substrate using silver paint and copper wire. This contact area was later covered with nonconducting epoxy resin to isolate it from the electrolyte solution. A glass rod was placed over the copper wire for better handling. The electrochemical setup for impedance measurements consisted of three electrodes: the working electrode (individual α-Bi_2O_3 and β-Bi_2O_3 film), a platinum wire used as counter electrode, and a standard saturated calomel electrode (SCE). The photocurrents were measured using a Solartron 1287 potentiostat. Mott-Schottky analyses were performed with a Solartron 1255B frequency response analyzer under control by ZPLOT software. The solution containing 0.5 M Na_2SO_4 aqueous solution was used as the electrolyte. A 300 W Xe lamp was utilized as a light source.

3. Results and discussion

The XRD patterns of the as-prepared samples are shown in Fig. 1. The product calcined at 300 °C using the precursors at the hydrothermal temperature of 120 °C can be indexed to well crystallized β-Bi_2O_3 structure (PDF NO. 27-50) with the major peaks at 2θ = 27.94, 31.76, 32.69, 46.22, 54.27, 55.48, 57.75, and 66.12°, corresponding to the diffractions of the (2 0 1), (0 0 2), (2 2 0), (2 2 2), (2 0 3), (4 2 1), (4 0 2), and (4 0 0) plane of the tetragonal β-Bi_2O_3. However, metastable β-Bi_2O_3 changed gradually into α-Bi_2O_3 as the hydrothermal temperature increased. In the XRD pattern of the

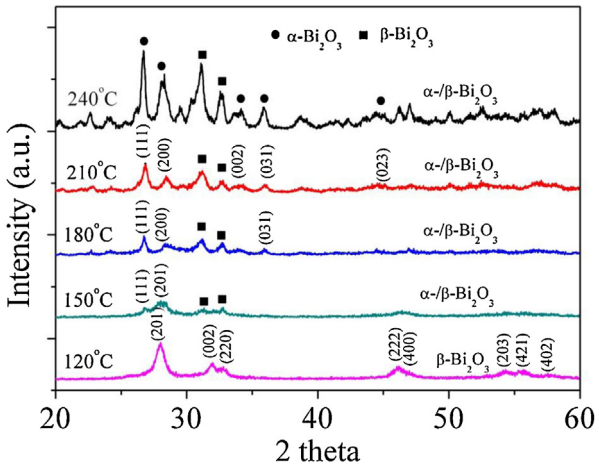

Fig. 1. The XRD patterns of the as-prepared Bi_2O_3 nanostructures using the precursors prepared at different temperatures.

product at 150 °C, the peaks of β-Bi_2O_3 decreased while the second phase of α-Bi_2O_3 (PDF NO.6-294) appeared, with the major peaks at 2θ = 25.75, 26.92, 33.03 and 33.94°, corresponding to the diffractions of the (0 0 2), (1 1 1), (1 2 1) and (0 3 1) plane of the monoclinic α-Bi_2O_3. Namely, the composites of α-Bi_2O_3 and β-Bi_2O_3 were obtained at the hydrothermal temperature of 150 °C. With the further increase of the hydrothermal temperature up to 180–240 °C, the major phase can be indexed to the monoclinic α-Bi_2O_3 (PDF NO.4-294) while a little amount of second phase can be recognized as the tetragonal β-Bi_2O_3 phase (PDF NO.18-244), indicating the formation of α–β phase heterojunction on Bi_2O_3. In addition, XPS signals of Bi 4f were observed at binding energies at around 164.2–164.1 eV (Bi $4f_{5/2}$) and 158.8–158.7 eV (Bi $4f_{7/2}$) ascribed to Bi^{3+} from XPS analysis, which is consistent with the previous reports of Bi_2O_3 powders [25], also indicating that the samples are containing α-Bi_2O_3 and β-Bi_2O_3. Thus, the controllable temperature of hydrothermal process played a very important role in this synthesis of α–β phase heterojunction on Bi_2O_3 that is considering the high photocatalytic activity of the as-prepared samples.

To obtain information about the particles morphology, some selected powders were investigated by field-emission scanning electron microscopy (FE-SEM). The SEM images of the synthesized bismuth based cluster as the precursors prepared by a benzyl alcohol assisted hydrothermal process at 120–240 °C were shown in Fig. 2. The SEM results clearly indicate that the calcined sample was composed of a large number of sheet after the hydrothermal reaction at 120 °C, while the product consists of many of sheets containing a little amount of nanowires at 150 °C (Fig. 2a and b). Furthermore, with increasing hydrothermal temperature up to 210–240 °C, the SEM images show the as-prepared samples consist of a great number of nanowires and parts of nanocrystals, as shown in Fig. 2c and d. From the results reported so far, it becomes obvious that the ratio of α–β phase heterojunction on Bi_2O_3 is mainly controlled by the hydrothermal temperature.

Further information was obtained by TEM analysis for the as-prepared α–β phase heterojunction on Bi_2O_3 samples (Fig. 3). Among the hydrothermal synthesis at 90–120 °C, the β-Bi_2O_3 products consist of sheets with landscape dimension of 100 nm–2 μm, as shown in Fig. 1S. The in-plane surfaces of the β-Bi_2O_3 sheets lies on {0 0 1} facet, indicating these β-Bi_2O_3 sheets with a high percentage of reactive {0 0 1} facets. With increasing hydrothermal temperature up to 150 °C, the sample is composed of α-Bi_2O_3 nanorods with heavy aggregates and some of β-Bi_2O_3 nanocrystals, which is in agreement with the results from XRD analysis. With further increasing hydrothermal temperature between 180 and 240 °C, the as-prepared products are composed of a great number of uniform nanowires with the average diameter below 50 nm, coupling with a little amount of β-Bi_2O_3 nanocrystals, as shown in Fig. 3 and Fig. 1S. From HRTEM images, it can be seen that small β-Bi_2O_3 nanocrystals are sporadically patched onto the surface of the original single-crystalline α-Bi_2O_3 nanowire, resulting in the exposure of both α and β phases on the surface. Moreover, it is observed that the phase junction between α-Bi_2O_3 and β-Bi_2O_3 is composed of well-matched lattice fringes between the (1 1 1) plane of α-Bi_2O_3 and the (0 0 1) plane of β-Bi_2O_3 (Fig. 3b). In addition, the selected area electron diffraction (SAED) pattern is shown in Fig. 3c and

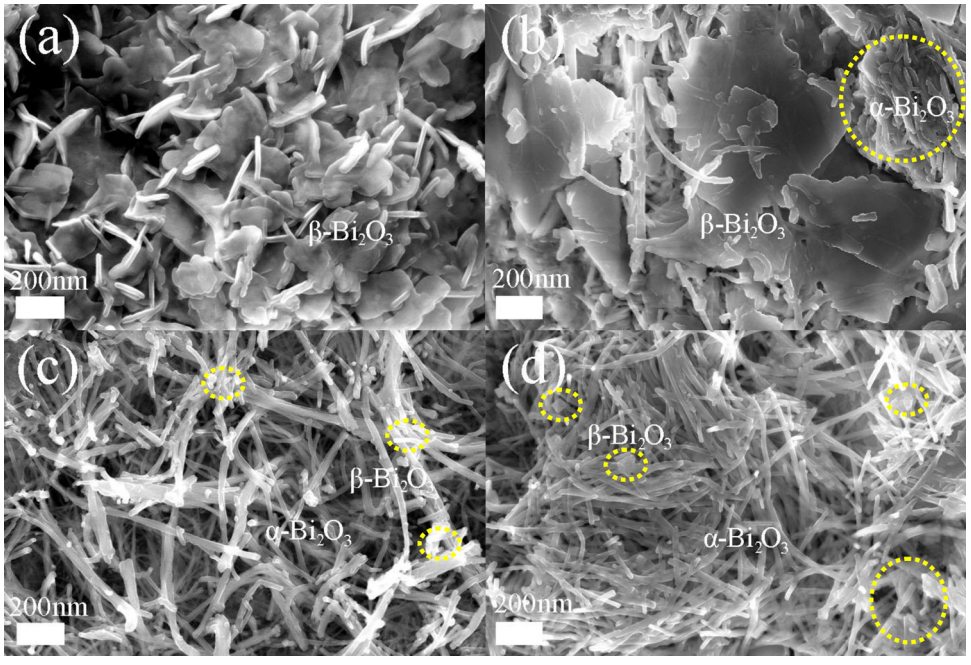

Fig. 2. The SEM images of the as-prepared products using the precursors prepared at various temperatures after calcinations. (a) 120 °C, (b) 150 °C, (c) 210 °C and (d) 240 °C.

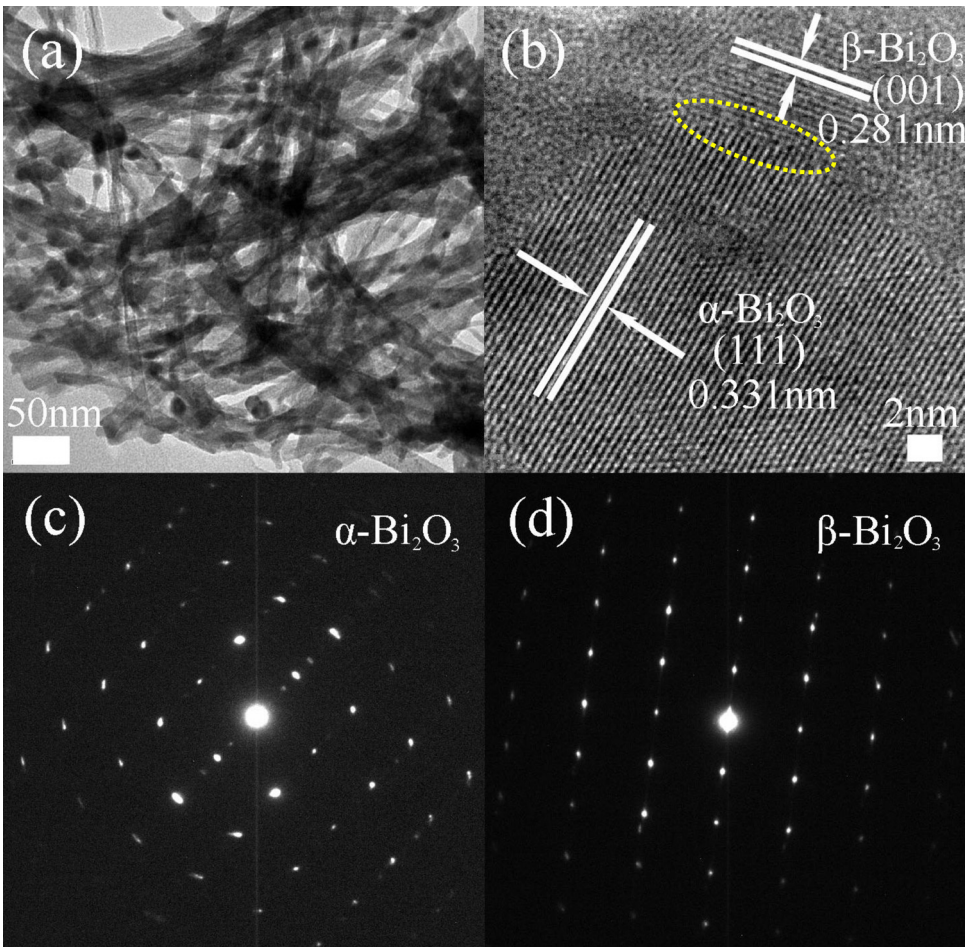

Fig. 3. The TEM (a) and HRTEM (b) images of the α–β phase heterojunction on Bi_2O_3 nanostructures using the precursors prepared at 210 °C. The SAED patterns from (c) α-Bi_2O_3 and (d) β-Bi_2O_3.

d, which also indicates a single-crystal structure for individual α-Bi_2O_3 and β-Bi_2O_3. All results clearly demonstrate that atomically well-defined α–β phase junctions of Bi_2O_3 can be tailor-designed and obtained by phase transformation.

Full nitrogen sorption isotherms of the β-Bi_2O_3 sheets and the α–β phase heterojunction on Bi_2O_3 samples, were measured to gain the information about the specific surface area, as shown in Fig. 4. The specific surface area the α–β phase heterojunction on Bi_2O_3 nanostructures using the precursors prepared at 210 °C was calculated to be 44 $m^2\ g^{-1}$ by the BET equation, as shown in Fig. 4. The corresponding Barrett Joyner Halenda (BJH) analyses (the inset in Fig. 4) for the α–β phase heterojunction on Bi_2O_3 nanostructures using the precursors prepared at 210 °C exhibit that most of the pores fall into the size range from 5 to 60 nm. These pores presumably arise from the spaces among the composites within the α–β phase heterojunction on Bi_2O_3 nanostructures. However, as shown in Fig. 4, the specific surface area of the β-Bi_2O_3 nanostructures was calculated to be 9 $m^2\ g^{-1}$, which is lower that of the α–β phase heterojunction on Bi_2O_3 nanostructures using the precursors prepared at 210 °C. The high surface area and mesoporous structure of the Bi_2O_3 junction nanostructures will lead to the enhanced photocatalytic performance of Bi_2O_3 nanostructures.

The optical absorption of the Bi_2O_3 nanostructures was measured by UV–vis diffuse reflection spectroscopy, and the results are shown in Fig. 5. The absorbance edge of the as-prepared Bi_2O_3 samples located approximately in the wave length range from 400 to 550 nm. The band gap energies of the as-prepared Bi_2O_3 samples using the bismuth based clusters prepared at 120–240 °C, is determined from a plot of $(ahv)^2$ vs energy (hv) (Fig. 5) and are found to be about 2.40–2.80 eV, respectively. Namely, the band gap of α–β phase heterojunction on Bi_2O_3 and β-Bi_2O_3 nanostructures and is found to be 2.71 and 2.48 eV. Utilizing visible light for driving photocatalytic reactions is a key challenge and visible light absorption of a material is a prerequisite for visible light activity.

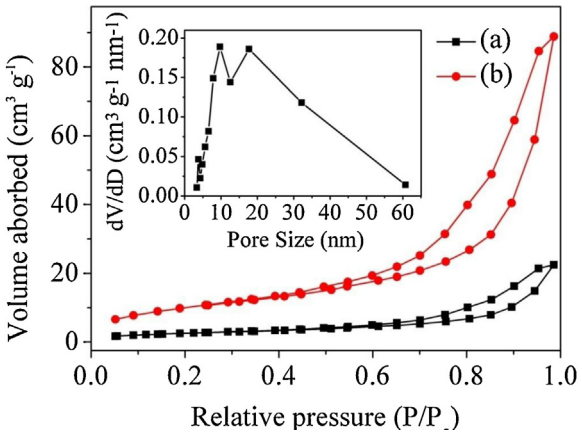

Fig. 4. Full nitrogen sorption isotherms of (a) β-Bi_2O_3 and (b) α–β phase heterojunction on Bi_2O_3 nanostructures using the precursors prepared at 210 °C. The inset is the corresponding pore-size distribution of α-/β-Bi_2O_3 heterojunction using the precursors prepared at 210 °C.

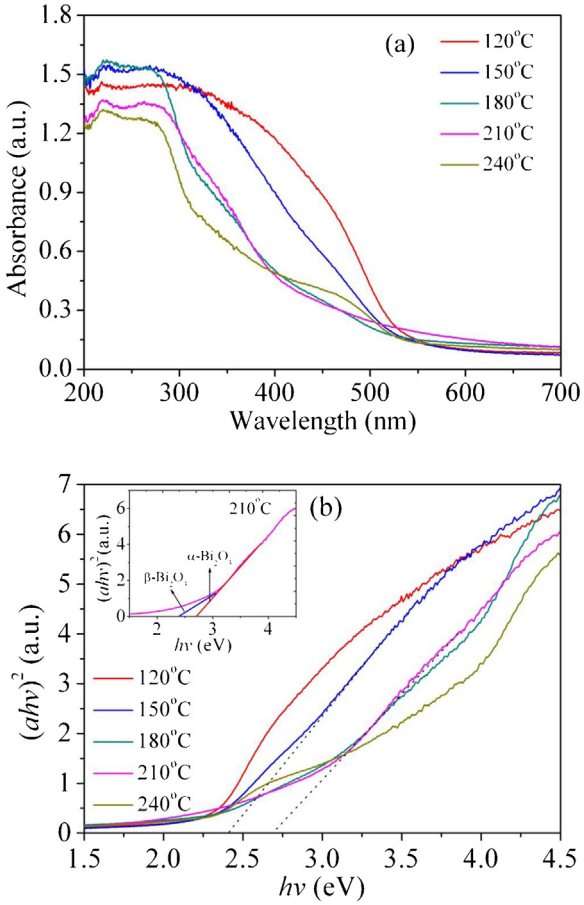

Fig. 5. (a) The UV–vis spectra of the products using the precursors prepared at different temperatures after calcinations. (b) Plots of $(ahv)^2$ vs energy (hv) for the band gap energies.

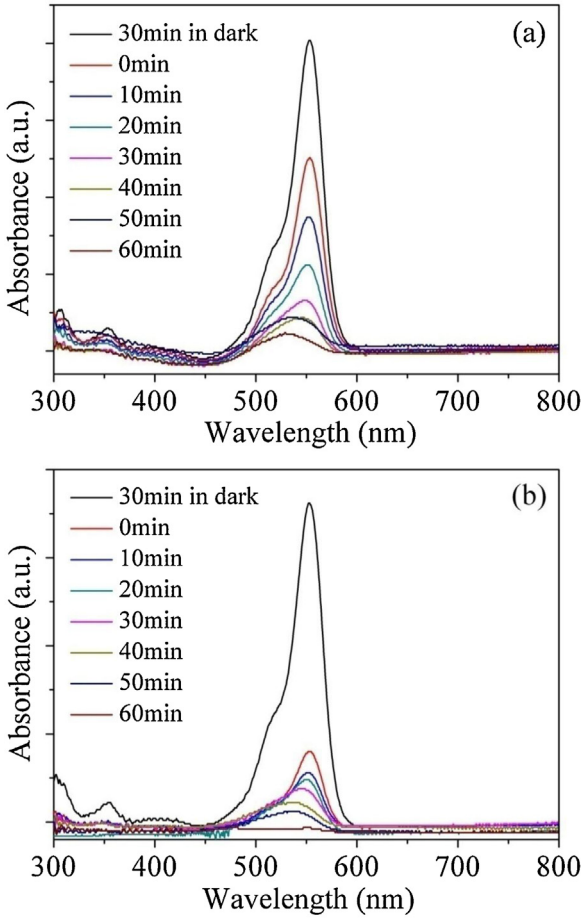

Fig. 6. UV–vis spectra changes in RhB degradation with (a) β-Bi_2O_3 and (b) α–β phase heterojunction on Bi_2O_3 nanostructures using the precursors prepared at 210 °C under visible-light irradiation.

The photocatalytic activities of the as-prepared samples were evaluated by monitoring the degradation of rhodamine B (RhB) and methyl orange (MO) in an aqueous solution under visible light irradiation, respectively. The time-dependent UV–vis absorption spectra of RhB dye during the irradiation are displayed in Fig. 6. It can be seen clearly that the maximum absorbance of 550 nm decreases greatly after irradiation in 60 min for the α-Bi_2O_3 and β-Bi_2O_3 samples. Fig. 7 and Fig. 3S show the photodegradation of RhB and MO dyes as a function of irradiation time. For the degradation of RhB and MO dye molecules, the photocatalytic performance of Bi_2O_3 nanostructures using the precursors increase with increasing hydrothermal temperatures from 90 to 210 °C. The best photocatalytic degradation efficiencies of α–β phase heterojunction on Bi_2O_3 nanowires using the precursors prepared at 210 °C were achieved about 98% for RhB dye molecule after irradiation for 60 min and around 96% for MO dye after irradiation for 15 min. In comparison, the degradation efficiencies of β-Bi_2O_3 sheets only reached about 85% for RhB dye molecule after irradiation for 60 min and around 79% for MO dye after irradiation for 15 min. While the photocatalytic activity of the sample decreases with increasing hydrothermal temperature up to 240 °C. In addition, the blank experiments were also carried out in the presence of the α–β phase heterojunction on Bi_2O_3 using the precursors prepared at 210 °C and β-Bi_2O_3 samples without irradiation or in the presence of irradiation without the α–β phase heterojunction and β-Bi_2O_3 samples, from which we can observe that there is no apparent change for the degradation of RhB and MO dyes under visible light irradiation in the absence of photocatalysts. Besides, the adsorption capacities of RhB molecules on Bi_2O_3 nanostructures using the precursors at 90, 120, 150, 180, 210 and 240 °C are approaching 95.8%, 68.7%, 60.8%, 38.1%, 30.2% and 47.7%, respectively. And the adsorption capacities of MO molecules on Bi_2O_3 nanostructures using the precursors at 90, 120, 150, 180, 210 and 240 °C are approaching 50.0%, 47.6%, 42.6%, 29.5%, 23.8% and 35.0%, respectively, which is ascribed to the high surface area of the α–β

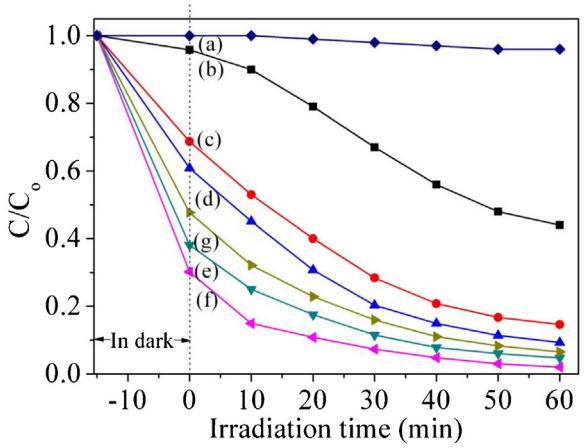

Fig. 7. Visible-light photocatalytic degradation of RhB solution of the products using the precursors prepared at different temperatures after calcinations. (a) RhB without catalyst, (b) 90°, (c) 120 °C, (d) 150 °C, (e) 180 °C, (f) 210 °C and (g) 240 °C.

phase heterojunction on Bi_2O_3 and β-Bi_2O_3 samples. In order to investigate the details of the photocatalytic process, the mineralization efficiencies (TOC tests) of the photodegradation for RhB (after 60 min) and MO (after 15 min) solution for the α–β phase heterojunction on Bi2O3 using the precursors prepared at 210 °C were found to be 72% and 66%, respectively. However, the photodegradation rates of RhB (after 60 min) and MO (after 15 min) solution were achieve 98% and 96%, indicating that the mineralization rate was slower than that of discoloration of dyes (Fig. 4S). In addition, it is well known that the photocatalytic performance of β-Bi_2O_3 is better than that of α-Bi_2O_3, which was explained by electronic structure calculations and experimental evidence [26–30]. Compared to the previous reports [21–34], the as-prepared α–β phase heterojunction on Bi_2O_3 nanostructures using the precursors prepared at 210 °C exhibited higher photocatalytic performance than individual α-Bi_2O_3 or β-Bi_2O_3 in the degradation of RhB and MO molecules.

Generally, the decomposition of the dye could be assigned to a pseudo-first-order kinetics reaction with a simplified Langmuir–Hinshelwood model when C_o is very small.

$$\ln\left(\frac{C_o}{C}\right) = kt$$

where k is the apparent first-order kinetics rate constant, and was determined from a linear fit to the data as shown in Fig. 8. Clearly, the degradating kinetics rate of RhB molecules on Bi_2O_3 nanostructures using the precursors at 90, 120, 150, 180, 210 and 240 °C are approaching 0.01406, 0.02718, 0.03143, 0.03484, 0.04343 and 0.03285, respectively. Besides, it is obvious that the kinetics rate of degradating RhB molecules on Bi_2O_3 nanostructures using the precursors at 90, 120, 150, 180, 210 and 240 °C are approaching 0.03801, 0.06261, 0.07061, 0.08308, 0.12835 and 0.07639, respectively. In addition, the photodegradation of RhB and MO dyes that were monitored over five cycles under a certain irradiation time. After each cycle, the photocatalytic efficiency exhibited only a slight decrease and no significant loss of activity after the decomposition was repeated five consecutive times (Fig. 5S), indicating that α–β phase heterojunction on Bi_2O_3 nanowire was an efficient and stable visible-light photocatalyst. Furthermore, the main active species in the visible-light-driven photocatalytic process were examined in the experiments of in situ capture of active pieces. The photodegradation of RhB solution for α–β phase heterojunction on Bi_2O_3 nanowires was slightly inhibited by the addition of t-BuOH (hydroxyl radicals scavenger) under visible light irradiation, indicating that the free hydroxyl radicals were not the major active oxidizing species in the photocatalytic process, as shown in Fig. 6S. However, it was intensively suppressed when EDTA (holes scavenger) was introduced. This indicates that holes were the main active oxidizing species involved in the photoreaction process, which is consistent with the previous reports [36,37].

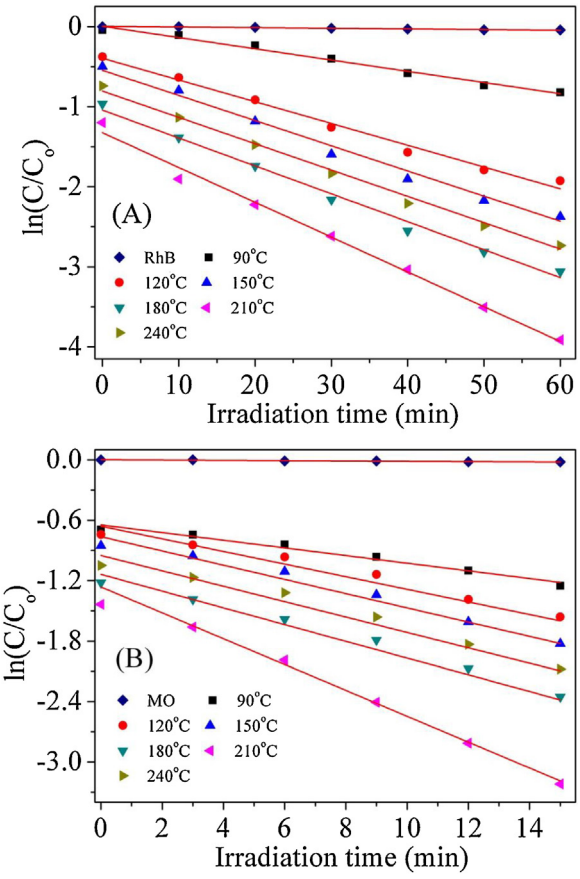

Fig. 8. Visible-light photocatalytic kinetic rates of (A) RhB and MO (B) solution of the products using the precursors prepared at different temperatures after calcinations.

Generally, the better photocatalytic performance of β-Bi_2O_3 has been shown in the previous works [21–34], which is ascribed to the wide absorbance in the visible light region from electronic structure calculation and UV–vis measurement. However, the unusual superior catalytic activity of α–β phase heterojunction on Bi_2O_3 was exhibited in this work. In order to have an in-depth understanding of the unique catalytic performance of α–β phase heterojunction on Bi_2O_3, the several points for Bi_2O_3 nanostructures were shown. As we know, the morphology, phase component, shape, and size could play important roles on the photocatalytic efficiency. As indicated in Table 1, the surface properties of the synthesized α–β phase heterojunction on Bi_2O_3, possesses a higher surface area and pore volume, providing the possibility for the efficient diffusion and transportation of the degradable organic molecules and hydroxyl radicals in photochemical reaction. Furthermore, the possible transfer routes of the photo-generated electrons and holes were also introduced to explain the enhanced photocatalytic activity using the conduction band minimum (CBM) and valence band maximum (VBM) potentials of α-Bi_2O_3 and β-Bi_2O_3. The band structures of α-Bi_2O_3 and β-Bi_2O_3 were further examined by Mott-Schottky measurements. The flat-band potentials (E_{fb})of α-Bi_2O_3 and β-Bi_2O_3 are estimated to be −0.46 V and −0.15 V vs. SCE (−0.22 V and +0.09 V vs. NHE) by Mott–Schottky analysis (Fig. 9). E_{fb} is strongly related to the bottom of the E_{cb} and is considered to be located just under the E_{cb} for the semiconductors indicating that the flat band potential of α-Bi_2O_3 is more negative than that of β-Bi_2O_3, and the valence band potential of β-Bi_2O_3 is more positive than that of α-Bi_2O_3, as shown in Fig. 9. The mechanism of the enhancement of photocatalytic activity is illustrated in Fig. 10. A scheme for

Table 1
Quantitative phase composition and physicochemical properties of various Bi_2O_3 samples.

Samples	Synthetic temperature	S_{BET} [$m^2\ g^{-1}$][a]	RhB degradation kinetic rate [$k\ min^{-1}$][b]	MO degradation kinetic rate [$k\ min^{-1}$][b]
S1	90 °C	3	0.01406	0.03801
S2	120 °C	9	0.02718	0.06261
S3	150 °C	12	0.03143	0.07061
S4	180 °C	22	0.03484	0.08308
S5	210 °C	44	0.04343	0.12835
S6	240 °C	18	0.03285	0.07639

Physicochemical properties of various bismuth oxide samples.
[a] Measurement from specific surface area.
[b] Photocatalytic degradation kinetic rates of RhB and MO solution for various bismuth oxide samples under visible-light irradiation.

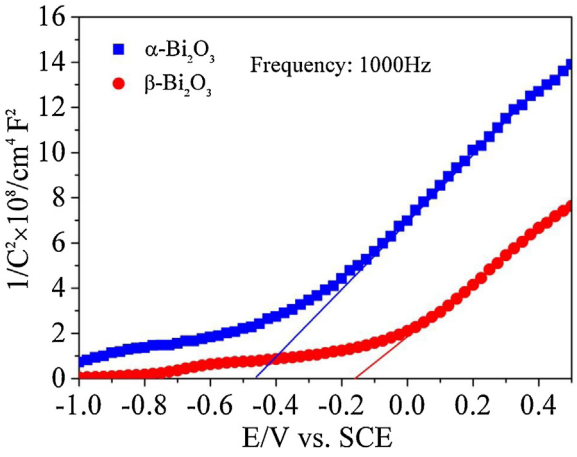

Fig. 9. Mott-Schottky plots obtained for the films electrodes prepared with and α-Bi_2O_3 and β-Bi_2O_3 in 0.5 M Na_2SO_4, and the ac amplitude is 10 mV and the frequency is 1000 Hz.

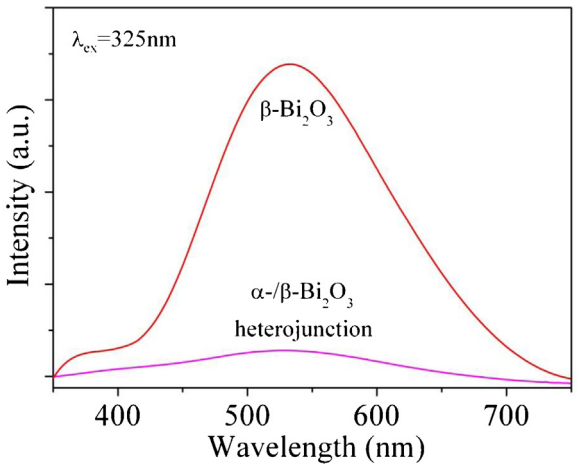

Fig. 11. Photoluminescence spectra of β-Bi_2O_3 and α-/β-Bi_2O_3 heterojunction nanowires using the precursors prepared at 210 °C, excited at the wavelength of 325 nm.

electron–hole separation and transport at the visible-light-driven heterojunction photocatalyst interface and in both semiconductors is shown in Fig. 10. Since the CB edge potential of α-Bi_2O_3 is more negative than that of β-Bi_2O_3 the photoinduced electrons on α-Bi_2O_3 surfaces transfer easily to β-Bi_2O_3 via the well developed interface. Similarly, the photoinduced holes on the β-Bi_2O_3 surface move to α-Bi_2O_3 due to the large difference in VB edge potentials retarding the recombination of the photoinduced electron–hole pairs in the α-/β-Bi_2O_3 heterojunction. Thus, the α-Bi_2O_3 coated on the surface of β-Bi_2O_3 could function as traps to capture the photoinduced holes and the heterojunction of α-/β-Bi_2O_3 could act as an active center for hindering the rapid recombination of photoinduced electron–hole pairs.

For semiconductors, the photoluminescence (PL) spectra is related to the transfer behavior of the photoinduced electrons and holes, so that it can reflect the separation and recombination of photoinduced charge carriers [38,39]. The PL spectra of the as-prepared β-Bi_2O_3 and α–β phase heterojunction on Bi_2O_3 nanostructures using the precursors prepared at 210 °C are shown in Fig. 11. The excitation wavelength is determined as 325 nm, and the β-Bi_2O_3 has a strong emission peak at about 533 nm. Furthermore, there was a small PL peak observed for α–β phase heterojunction on Bi_2O_3 nanostructures using the precursors prepared at 210 °C, indicating that the electron–hole pairs recombination is very slow. This is ascribed to the fact that α–β phase heterojunction on Bi_2O_3 nanostructures could prevent the direct recombination of electrons and holes, which is of great benefit for enhancing activity in the photocatalytic reaction.

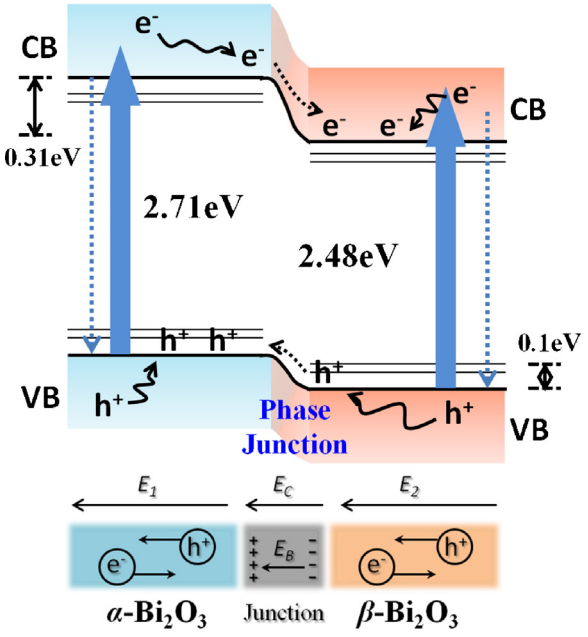

Fig. 10. Scheme for electron–hole separation and transport at the visible-light-driven heterojunction photocatalyst interface and in both semiconductors: E_C is the contact electric field for the two materials; E_B is the potential barrier in the interfacial depletion layer ($E_B < E_C$ during the photocatalytic reaction); E_1 and E_2 are the internal electric fields induced by the redistribution of the spatial charges in α-Bi_2O_3 and β-Bi_2O_3 particles, respectively.

4. Conclusion

Visible-light-responsive α–β phase heterojunction on Bi_2O_3 nanowires photocatalysts were prepared via a facile in situ hydrothermal process in assistance with the post-heat treatment route. XRD patterns revealed that the α–β phase heterojunction with the monoclinic α-Bi_2O_3 and the tetragonal β-Bi_2O_3 structure were obtained with increasing of the hydrothermal temperature. Within the reaction temperature, the morphology of as-prepared samples transformed progressively from β-Bi_2O_3 sheets to the α-/β-Bi_2O_3 nanowires. The exceptional photocatalytic performance of α–β phase heterojunction on Bi_2O_3 nanowire for the degradation of cationic rhodamine B and anionic methyl orange under visible-light irradiation is superior over that of β-Bi_2O_3 sheets, which is ascribed to the efficient charge separation and transfer across the α–β phase junction. The phase-junction approach will open new avenues for the development of efficient photocatalysts for environmental remediation and energy conversion.

Acknowledgements

This work was supported by National Science Foundation of China (No. 51102015, 21071014 and 51004008), the Fundamental Research Funds for the Central Universities (No. FRF-AS-11-002A and FRF-TP-12-023A), Research Fund for the Doctoral Program of Higher Education of China (No. 20110006120027), National High Technology Research and Development Program of China (863 Program, No. 2012AA062302), National Basic Research Program of China (973 Program, No. 2007CB613301), the Program for New

Century Excellent Talents in University (NCET-11-0577) and the 111 Project (B13004).

Appendix A. Supplementary data

Supplementary data associated with this article can be found, in the online version, at http://dx.doi.org/10.1016/j.apcatb.2013.05.050.

References

[1] X. Chen, S. Mao, Chem. Rev. 107 (2007) 2891.
[2] R. Kozhummal, Y. Yang, F. Güder, A. Hartel, X. Lu, U.M. Küçükbayrak, A. Mateo-Alonso, M. Elwenspoek, M. Zacharias, ACS Nano 6 (2012) 7133.
[3] A. Kudo, Y. Miseki, Chem. Soc. Rev. 38 (2009) 253.
[4] Y. Noda, B. Lee, K. Domen, J.N. Kondo, Chem. Mater. 20 (2008) 5361.
[5] G. Liu, H.G. Yang, X.W. Wang, L.N. Cheng, J. Pan, G.Q. Lu, H.M. Cheng, J. Am. Chem. Soc. 131 (2009) 12868.
[6] Q.J. Xiang, J.G. Yu, W.G. Wang, M. Jaroniec, Chem. Commun. 47 (2011) 6906.
[7] G. Liu, C.H. Sun, S.C. Smith, L.Z. Wang, G.Q. Lu, H.M. Cheng, J. Colloid Interface Sci. 349 (2010) 477.
[8] J.G. Yu, G.P. Dai, Q.J. Xiang, M. Jaroniec, J. Mater. Chem. 21 (2011) 1049.
[9] J.W. Tang, Z.G. Zou, J.H. Ye, Angew. Chem. Int. Ed. 43 (2004) 4463.
[10] W.J. Luo, Z.S. Yang, Z.S. Li, J.Y. Zhang, J.G. Liu, Z.Y. Zhao, Z.Q. Wang, S.C. Yan, T. Yu, Z.G. Zou, Energy Environ. Sci. 4 (2011) 4046.
[11] L. Zhou, W.Z. Wang, S.W. Liu, J. Mol. Catal. A: Chem. 252 (2006) 120.
[12] J.G. Hou, R. Cao, Z. Wang, S.Q. Jiao, H.M. Zhu, J. Hazard. Mater. 217–218 (2012) 177.
[13] J.G. Hou, Z. Wang, S.Q. Jiao, H.M. Zhu, CrystEngComm 14 (2012) 5923.
[14] X.Q. Zhu, J.L. Zhang, F. Chen, Appl. Catal. B 102 (2011) 316.
[15] J.G. Hou, R. Cao, S.Q. Jiao, H.M. Zhu, R.V. Kumar, Appl. Catal. B 104 (2011) 399.
[16] J.G. Hou, Y.F. Qu, D. Krsmanovic, C. Ducati, D. Eder, R.V. Kumar, Chem. Commun. 26 (2009) 3937.
[17] J.G. Hou, Y.F. Qu, D. Krsmanovic, C. Ducati, D. Eder, R.V. Kumar, J. Mater. Chem. 20 (2010) 2418.
[18] J.G. Hou, R. Cao, Z. Wang, S.Q. Jiao, H.M. Zhu, J. Mater. Chem. 11 (2011) 7296.
[19] L.S. Zhang, W.Z. Wang, Z.L. Zhou, Small 3 (2007) 1618.
[20] J.G. Hou, Z. Wang, C. Yang, W.L. Zhou, S.Q. Jiao, H.M. Zhu, J. Phys. Chem. C 117 (2013) 5132.
[21] L.S. Zhang, W.Z. Wang, J. Yang, Z.G. Chen, W.Q. Zhang, L. Zhou, S.W. Liu, Appl. Catal. A 308 (2006) 105.
[22] M. Drache, P. Roussel, J.P. Wignacourt, Chem. Rev. 107 (2007) 80.
[23] H. Abdul, M. Tiziano, G. Valentina, J. Am. Chem. Soc. 130 (2008) 9658.
[24] J.C. Yu, A.W. Xu, L.Z. Zhang, R.Q. Song, L. Wu, J. Phys. Chem. B 108 (2004) 64.
[25] H.F. Cheng, B.B. Huang, J.B. Lu, Z.Y. Wang, B. Xu, X.Y. Qin, X.Y. Zhang, Y. Dai, Phys. Chem. Chem. Phys. 12 (2010) 15468.
[26] H.W. Kim, Thin Solid Films 516 (2008) 3665.
[27] H. Zhang, P. Wu, Y. Li, L.F. Liao, Z. Fang, X.H. Zhong, ChemCatChem 2 (2010) 1115.
[28] J.K. Reddy, B. Srinivas, V.D. Kumari, M. Subrahmanyam, ChemCatChem 1 (2009) 492.
[29] J. In, I. Yoon, K. Seo, J. Park, J. Choo, Y. Lee, B. Kim, Chem. Eur. J. 17 (2011) 1304.
[30] A. Hameed, T. Montini, V. Gombac, P. Fornasiero, J. Am. Chem. Soc. 9 (2008) 9659.
[31] M. Muruganandham, R. Amutha, G.J. Lee, S.H. Hsieh, J.J. Wu, M. Sillanpää, J. Phys. Chem. C 116 (2012) 12906.
[32] R. Chen, Z.R. Shen, H. Wang, H.J. Zhou, Y.P. Liu, D.T. Ding, T.H. Chen, J. Alloys Compd. 509 (2011) 2588.
[33] K. Brezesinski, R. Ostermann, P. Hartmann, J. Perlich, T. Brezesinski, Chem. Mater. 22 (2010) 3079.
[34] Y. Wang, S.H. Li, X.R. Xing, F.Z. Huang, Y.H. Shen, A.J. Xie, X.F. Wang, J. Zhang, Chem. Eur. J. 17 (2011) 4802.
[35] J.G. Hou, C. Yang, Z. Wang, S.Q. Jiao, H.M. Zhu, Appl. Catal. B 129 (2013) 333.
[36] S.B. Zhu, T.G. Xu, H.B. Fu, J.C. Zhao, Y.F. Zhu, Env. Sci. Technol. 41 (2007) 6234–6239.
[37] G.L. Huang, S.C. Zhang, T.G. Xu, Y.F. Zhu, Env. Sci. Technol. 42 (2008) 8516–8521.
[38] J.G. Hou, Z. Wang, W.B. Kan, S.Q. Jiao, H.M. Zhu, J. Mater. Chem. 22 (2012) 7291.
[39] J.G. Hou, Z. Wang, S.Q. Jiao, H.M. Zhu, J. Hazard. Mater. 192 (2011) 1772.